RESEARCH ARTICLE

ADVANCED FUNCTIONAL MATERIALS
www.afm-journal.de

Harnessing Electron Delocalization for Enhanced Capacity and Stability in Heterostructured Cathode for All-Solid-State Thin-Film Battery

*Yongkun Yu, Sheng Cao, Chenxu Dong, Hanxiao Wang, Cheng Zhou, Zhiying Miao, Kaijian Yan, Minjian Gong, Liqiang Mai, and Xu Xu**

Due to the maturation of Internet of Things (IoT) technology, all-solid-state thin-film batteries (ATFBs) have become an optimal power source for microelectronic devices by virtue of their exceptional compatibility and ease of integration. Nevertheless, ATFBs face challenges related to the electron and ion transport properties of electrode materials, resulting in a limited specific capacity and comprehensive performance that often falls short of practical application requirements. Herein, a strategy of constructing V_2O_5-$Cu_2V_2O_7$ heterostructures is proposed with an electron delocalization interface via introducing copper heteroatom, which effectively improves the lithium storage capacity. Meanwhile, the construction of the built-in electric field and the electron delocalization effect enhance the electron and ion transport kinetics. Consequently, the initial discharge specific capacity of the heterostructured thin-film cathode is up to 76.4 µAh cm^{-2} µm^{-1} and exhibited ultra-high cycling stability over 4000 cycles in liquid half cells. Finally, benefiting from this high capacity and stable heterostructured cathode, a highly durable and flexible ATFB is further demonstrated. This work provides new ideas to further improve the energy density and cycling stability of thin-film cathodes and is expected to extend the potential applications in microelectronics.

1. Introduction

The advent of the Internet of Things (IoT) has ushered in a new epoch marked by the relentless advancement of electronic and information technologies, characterized by miniaturization and high integration.[1–3] This progression has led to a proliferation of micro-small autonomous wireless electronic devices interconnected via the Internet. Nevertheless, the development of suitable microenergy storage devices has emerged as a critical bottleneck in further advancing these miniaturized electronic devices.[4] All-solid-state thin-film batteries (ATFBs), fabricated using thin film deposition technology, are considered to be a promising option for energy storage in microscale electronic devices.[5–7] Therefore, they have gained prominence as a leading frontier in global scientific and technological arenas and have become pivotal to industrial development. However, ATFBs with limited energy storage capacity have a long and arduous road to meet the practical application requirements (0.1 µWh – 1 mWh) of typical microelectronic devices and portable electronic devices. Most ATFBs feature a lithium metal anode. Notably, compared to the high theoretical specific capacity (3860 mAh g^{-1}) of Li, the choice of cathode material is crucial, which significantly influences the battery's capacity. Despite the favorable electrochemical performance demonstrated by ATFBs utilizing widely used cathode materials like $LiCoO_2$ and $LiMn_2O_4$ for lithium-ion batteries (LIBs), the limited capacity poses challenges in meeting practical application requirements.[8–10]

Among the various cathode materials for LIBs, vanadium pentoxide (V_2O_5) with a high theoretical capacity of 442 mAh g^{-1} has been intensively studied as a cathode for LIBs.[11] V_2O_5 is a layered intercalation compound characterized by its distinct structural arrangement. It features layers composed of twisted $[VO_5]$ pyramidal coordination polyhedra, interconnected by weak van der Waals forces, imparting notable stability.[12] However, its widespread application in ATFBs is hindered by challenges such as sluggish ion diffusion (10^{-12} to 10^{-13} cm^2 s^{-1}) and poor electronic conductivity (10^{-7} to 10^{-6} S cm^{-1}). Additionally, in the

Y. Yu, S. Cao, C. Dong, H. Wang, C. Zhou, Z. Miao, K. Yan, M. Gong, L. Mai, X. Xu
State Key Laboratory of Advanced Technology for Materials Synthesis and Processing
International School of Materials Science and Engineering
Wuhan University of Technology
Wuhan, Hubei 430070, P. R. China
E-mail: xuxu@whut.edu.cn

X. Xu
Hubei Longzhong Laboratory
Wuhan University of Technology (Xiangyang Demonstration Zone)
Xiangyang, Hubei 441000, P. R. China

X. Xu
Zhongyu Feima New Material Technology Innovation Center (Zhengzhou) Co.
Ltd.
High Technology Industrial Development Zone
No. 60 Xuelan Road, Zhengzhou 450001, P. R. China

The ORCID identification number(s) for the author(s) of this article can be found under https://doi.org/10.1002/adfm.202423990

DOI: 10.1002/adfm.202423990

typical operating voltage range (2.0–4.0 V, corresponding theoretical specific capacity of 294 mAh g^{-1}), the capacity utilization of V_2O_5 as a cathode for ATFBs is very restricted, thereby significantly constraining its capability to function as a high-capacity cathode material in ATFBs configurations.[13,14] Substantial efforts have been directed toward enhancing the electrochemical performance of V_2O_5 thin-film cathode, including constructing nanostructure,[15] introducing vacancies,[13] and heteroatom doping.[16,17] Hyun-Suk Kim and co-workers[13] designed and prepared an amorphous V_2O_{5-x} cathode with oxygen vacancies, enhancing both ionic and electronic conductivities. David M. Stewart et al. reported a promising LVO cathode for thin-film cathode made by co-sputtering of V_2O_5 and Li_2O, achieving high capacity.[17] Nevertheless, the specific capacity and cycle stability are still unsatisfactory.

To enhance the capacity of ATFBs, a common strategy considered is increasing the electrode mass loading. Practically, elevated loadings typically result in sluggish kinetics.[18–20] Hence, an optimal thin-film cathode should ideally possess a high voltage range and capacity, coupled with excellent electron and ion conductivity to support rapid discharge at high rates. Achieving this ideal, however, poses significant challenges necessitating precise control over electrode structure and chemistry spanning atomic to micron scales. Recent studies about constructing heterostructure for vanadium oxide cathode materials have demonstrated an innovative and effective approach to enhancing capacity.[21–23] Heterostructure, in brief, is a composite of two or more different materials or crystal structures. When different materials form a heterogeneous interface, a built-in electric field is spontaneously generated due to differences in electron cloud distribution and work function.[24,25] This built-in electric field can greatly facilitate electron and ion transport. Under its influence, the electrons can move rapidly through the material, and the Li^+ can cross the interface more efficiently, realizing rapid insertion and deinsertion.[26] By designing and regulating the heterostructure, the electron and ion transport can be optimized, allowing the battery to maintain high capacity and excellent charging and discharging performance at high voltage, which will help it to be widely used in future electronic devices and other fields.

In this study, targeting the urgent need for high-capacity applications of ATFBs, we propose a strategy of introducing copper heteroatom in V_2O_5 by co-sputtering to in-situ form a V_2O_5-$Cu_2V_2O_7$ heterostructure. With Cu heteroatom introduced, the Li^+ storage capacity of the cathode has been viably elevated by leveraging the high voltage characteristics of V_2O_5 combined with the substantial capacity of CuO. The introduction of a built-in electronic field significantly boosts both charging/discharging efficiency and electrode stability. The density functional theory (DFT) calculations indicate the V_2O_5-$Cu_2V_2O_7$ nano-heterostructure induces the construction of the built-in electric field through the imbalanced charge distribution, simultaneously enabling a higher degree of electron delocalization, which further privileges the electronic conductivity, the adsorption energy and diffusion energy barriers for Li^+, and ultimately facilitates the charge transfer kinetics of Li^+ in the heterostructured cathode. As a consequence, the V_2O_5-$Cu_2V_2O_7$ cathode attained a reversible specific capacity of up to 76.4 µAh cm^{-2} $µm^{-1}$ and an impressive capacity retention of ≈93% after 4000 cycles at 20 µA cm^{-2} in the half-cells based on a liquid electrolyte and a Li-metal anode, illustrating the significant improvements in capacity and stability by the heterostructures. Ultimately, an ATFB based on the V_2O_5-$Cu_2V_2O_7$ heterostructured cathode is successfully fabricated, which demonstrates an outstanding specific capacity of up to 65.0 µAh cm^{-2} $µm^{-1}$ (5 µA cm^{-2}), good rate performance, and excellent flexibility.

2. Results and Discussion

2.1. Construction of V_2O_5-$Cu_2V_2O_7$ Heterostructure and Structural Characterizations

The fabrication procedure is briefly depicted in **Figure 1**. The pure V_2O_5, V_2O_5-$Cu_2V_2O_7$, and amorphous $Cu_2V_2O_7$ thin films were deposited by radio frequency (RF) magnetron sputtering through adjusting the power of the co-sputtered copper, named VO, VOC1, and VOC2. The magnetron sputtering power of 1 W, and 2 W for Cu were selected to prepare VOC1 and VOC2, respectively, followed by a post-annealing temperature of 573 K. During the low-temperature post-annealing process, VOC1 in situ forms a V_2O_5-$Cu_2V_2O_7$ heterostructure. Raman spectra and X-ray diffraction (XRD) were employed to identify bonding states, crystal structure, and phase evolution. As shown by the comparison of Raman spectra in Figure 1b, VO shows favorable crystallinity, and ten Raman bonds are observed at 122, 165, 215, 305, 321, 424, 503, 547, 725, and 1014 cm^{-1} respectively, in accordance with the signature Raman spectrum of α-V_2O_5.[27] For the VOC1 sample, new Raman bonds appear at 811 and 872 cm^{-1}, corresponding to the asymmetric stretching vibrational modes of V—O_3.[28] The V—O_1 stretching mode at 938 cm^{-1} of the β-$Cu_2V_2O_7$ has a severe redshift of ≈76 cm^{-1} with respect to α-V_2O_5, which is attributable to the strong electrostatic attraction between Cu—O attenuates the local force between V—O.[29] The VO sample in Figure 1c shows good diffraction peaks at 15.4°, 20.3°, 26.2°, and 31.1°, which can be indexed to the diffraction pattern of orthorhombic V_2O_5 (ICDD PDF no. 001–0359).[30] As compared to the VO, the XRD pattern of the VOC1 exhibits new peaks at ≈24.8°, 28.2°, 28.8°, and 29.0°, revealing a similar diffraction pattern as monoclinic $Cu_2V_2O_7$ (ICDD PDF no. 073–1032).[31] It is important to note that both the Raman spectrum and XRD indicate that VOC2 is a typical amorphous structure, which is due to the excessive ratio of the Cu heteroatoms resulting in the need for $Cu_2V_2O_7$ to crystallize at higher temperatures (typically ≥773 K). Upon increasing the annealing temperature to 773 K, the VOC2 sample presented similar Raman peaks of CuO, while Raman characteristic peaks and XRD diffraction peaks matching $Cu_2V_2O_7$ were also observed, indicating the excessive introduction of Cu atoms (Figures S1 and S2, Supporting Information). To further study the elemental content in VOC1, the energy dispersive X-ray spectrum (EDS) of the heterostructures was collected and shown in Figure 1e and Figure S3 (Supporting Information). The proportion of Cu/V is 0.46, demonstrating the effective introduction of Cu heteroatoms and the formation of a biphasic composition. Alternatively, X-ray photoelectron spectroscopy (XPS) reveals the Cu content evolution of each sample as well as the elemental valence state of VOC1 in Figure 1d,f,g.

The surface morphologies of different samples were examined by field-emission scanning electron microscopy (FESEM). As il-

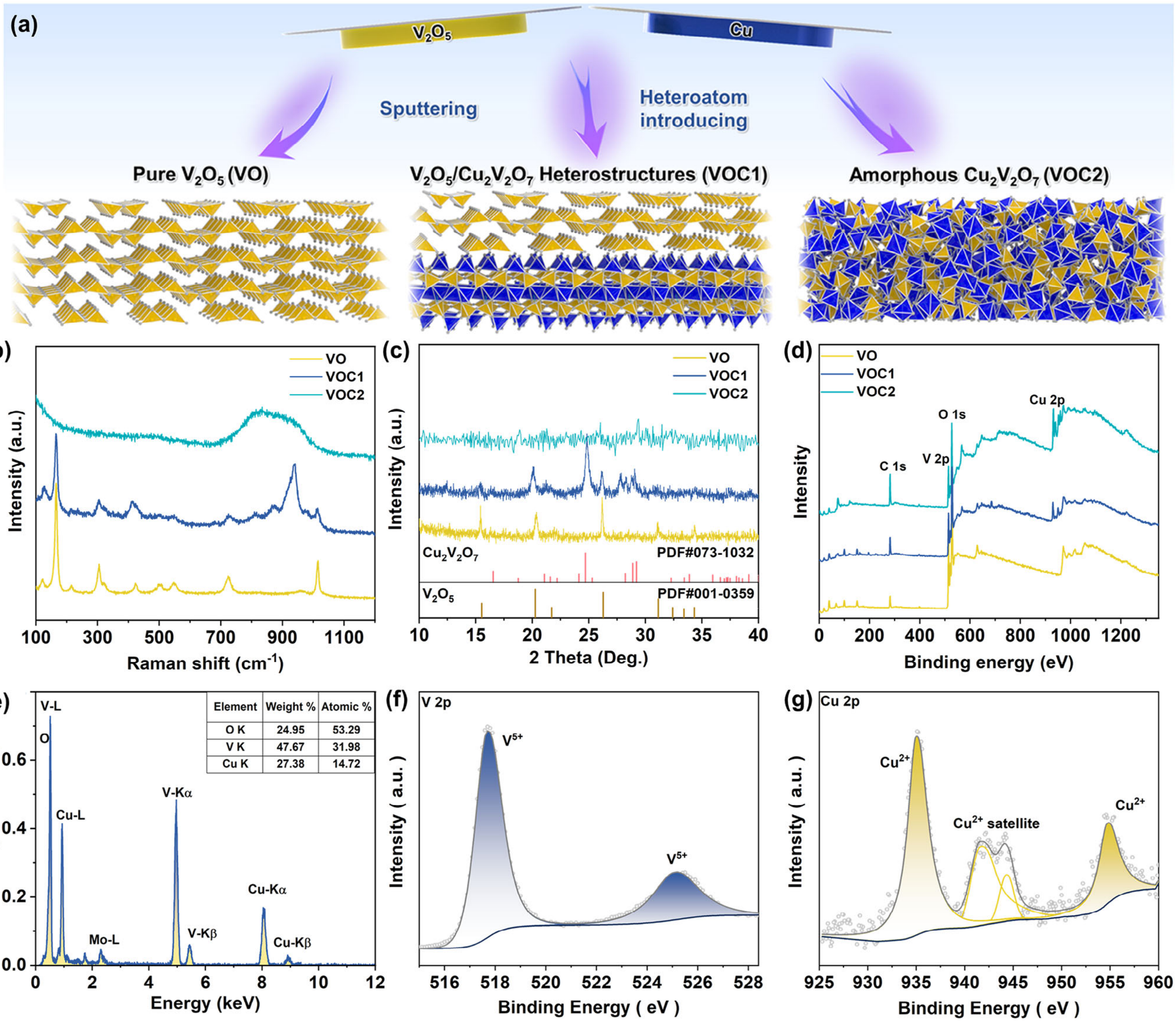

Element	Weight %	Atomic %
O K	24.95	53.29
V K	47.67	31.98
Cu K	27.38	14.72

Figure 1. a) Schematic representation depicting the process of fabricating VO, VOC1, and VOC2 thin films by magnetron sputtering. b) Raman spectra, c) XRD patterns, and d) XPS spectra of VO, VOC1, and VOC2 thin films. e) STEM-EDS spectrum, f) V 2p, and g) Cu 2p core-level XPS spectrum of VOC1 thin film.

lustrated in Figure S4a–c (Supporting Information), the Cu introduction not only induced the formation of $Cu_2V_2O_7$ but also refined the surface roughness, resulting in a reduction of film porosity. Surface mass spectrometry results from the time-of-flight secondary ion mass spectrometry (TOF-SIMS) also provide further testimony to the homogeneous elemental distribution on the film surface. The cross-sectional FESEM images of VO, VOC1, and VOC2 thin films are presented in **Figures** 2a and S5a,b (Supporting Information), which illustrate that the corresponding thicknesses of different films are 300, 300, and 420 nm, respectively. Notably, the prerequisite for the deposition rate to be proportional to the power applied to the target is that the voltage is high enough to energize the working gas ions in the electric field sufficiently to exceed the target's "sputtering energy threshold".[32,33] This threshold was clearly not exceeded during the VOC1 deposition process, so the sputtering rate was low and the heteroatoms introduction was minimal. In addition, Cu occupies $[VO_6]$ octahedral interlayer vacancies in $Cu_2V_2O_7$ without drastic volume changes.[34] Thus, VOC1 at lower Cu co-sputtering power (1 W) does not cause significant variation in film thickness with a hint of heteroatoms introduced, which is pivotal for the attainment of high-density films.

In order to have an intensive study of the heterostructure and the distribution, high-resolution transmission electron microscopy (HRTEM) was employed for structural analysis. Figure S6 (Supporting Information) presents a low magnification high-angle annular dark field (HAADF)-STEM image of the VOC1 sample, which reveals that the film consists of irregularly shaped nanograins. HRTEM images of the V_2O_5-$Cu_2V_2O_7$ heterostructure as shown in Figure 2d, where $Cu_2V_2O_7$ nanodomain (blue area) with a diameter of ≈10 nm is embedded in the layered V_2O_5

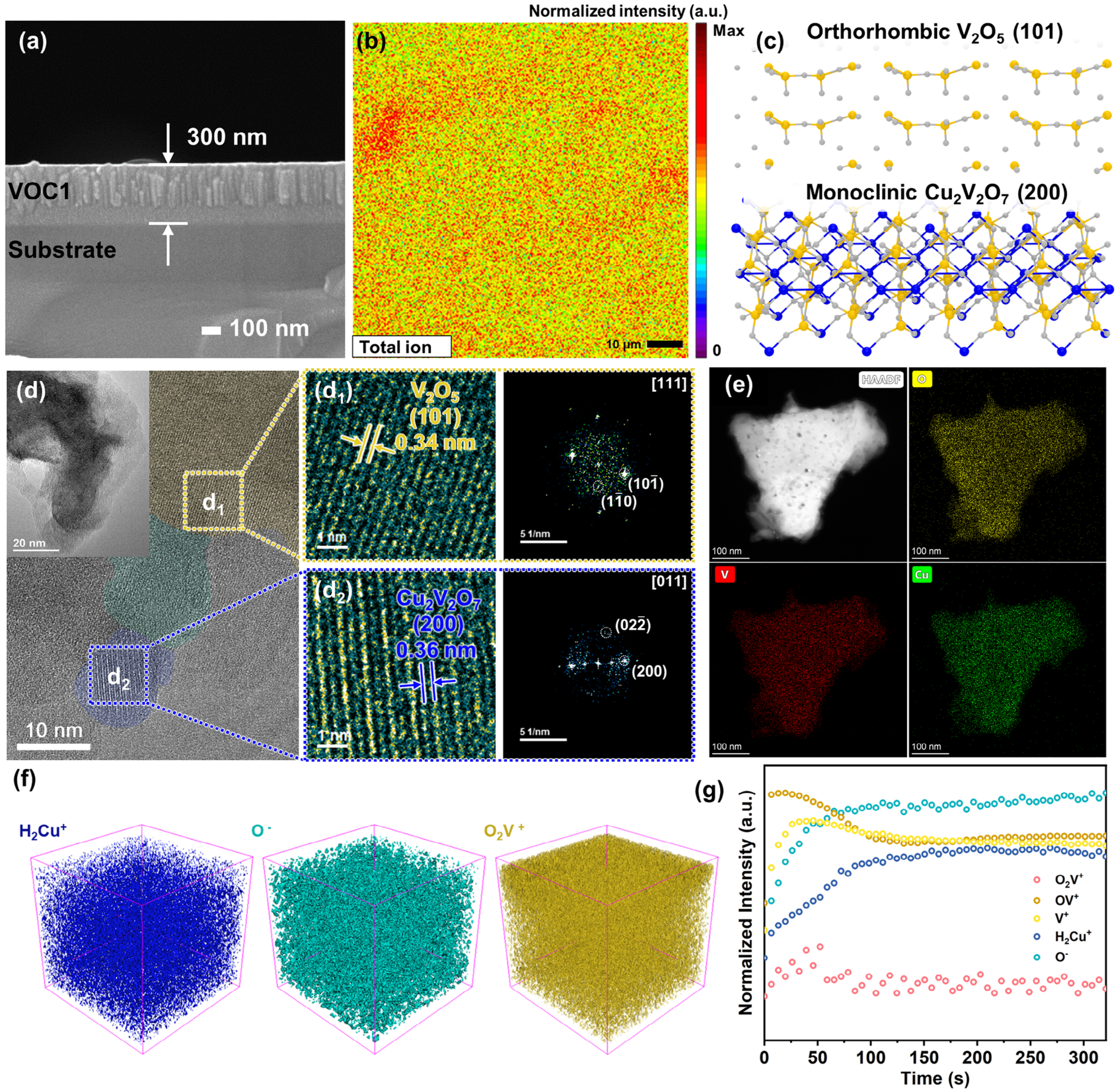

Figure 2. a) Cross-sectional FESEM image, and b) TOF-SIMS surface spectral distribution of VOC1 thin film. c) Crystal structures of orthorhombic V_2O_5 toward (101) plane and monoclinic $Cu_2V_2O_7$ toward (200) plane. d) HRTEM image of the V_2O_5-$Cu_2V_2O_7$ heterostructure. The yellow boxed portion corresponds to the V_2O_5 toward (101) plane while the blue boxed portion represents the presence of the monoclinic $Cu_2V_2O_7$ toward (200) plane. e) HAADF-STEM image and corresponding elemental mapping images, f) 3D reconstruction images of sputtered volume for the H_2Cu^+, O^-, and O_2V^+ fragment in the VOC1, and g) corresponding depth profiling curves.

matrix (yellow area), separated by a portion of the transition region (green area). The lattice fringes of 0.34 nm within the enlarged yellow square of Figure $2d_1$ correspond to (101) plane of V_2O_5, while the lattice fringes of 0.36 nm corresponding to (200) plane of $Cu_2V_2O_7$ are shown in Figure $2d_2$. Ideal structure models of α-V_2O_5 toward (101) plane and β-$Cu_2V_2O_7$ toward (200) plane (Figure 2c) were plotted to present a more intuitive illustration for the intergrowth of α-V_2O_5 and β-$Cu_2V_2O_7$ phases and the formation of the heterostructure.

To have a more intimate understanding of the elemental and structural distribution within the bulk phase of VOC1, TEM-EDS and TOF-SIMS were exploited. The EDS (Figure 2e) and TOF-SIMS surface spectral distribution (Figure 2b; Figure S7, Supporting Information) results indicate a uniform elemental distribution, whereas TOF-SIMS depth profiling of the films reveals that the film surfaces are depleted in Cu and enriched in V, which become progressively more homogeneous with depth, as 3D reconstruction images of sputtered volume for the H_2Cu^+, O_2^-,

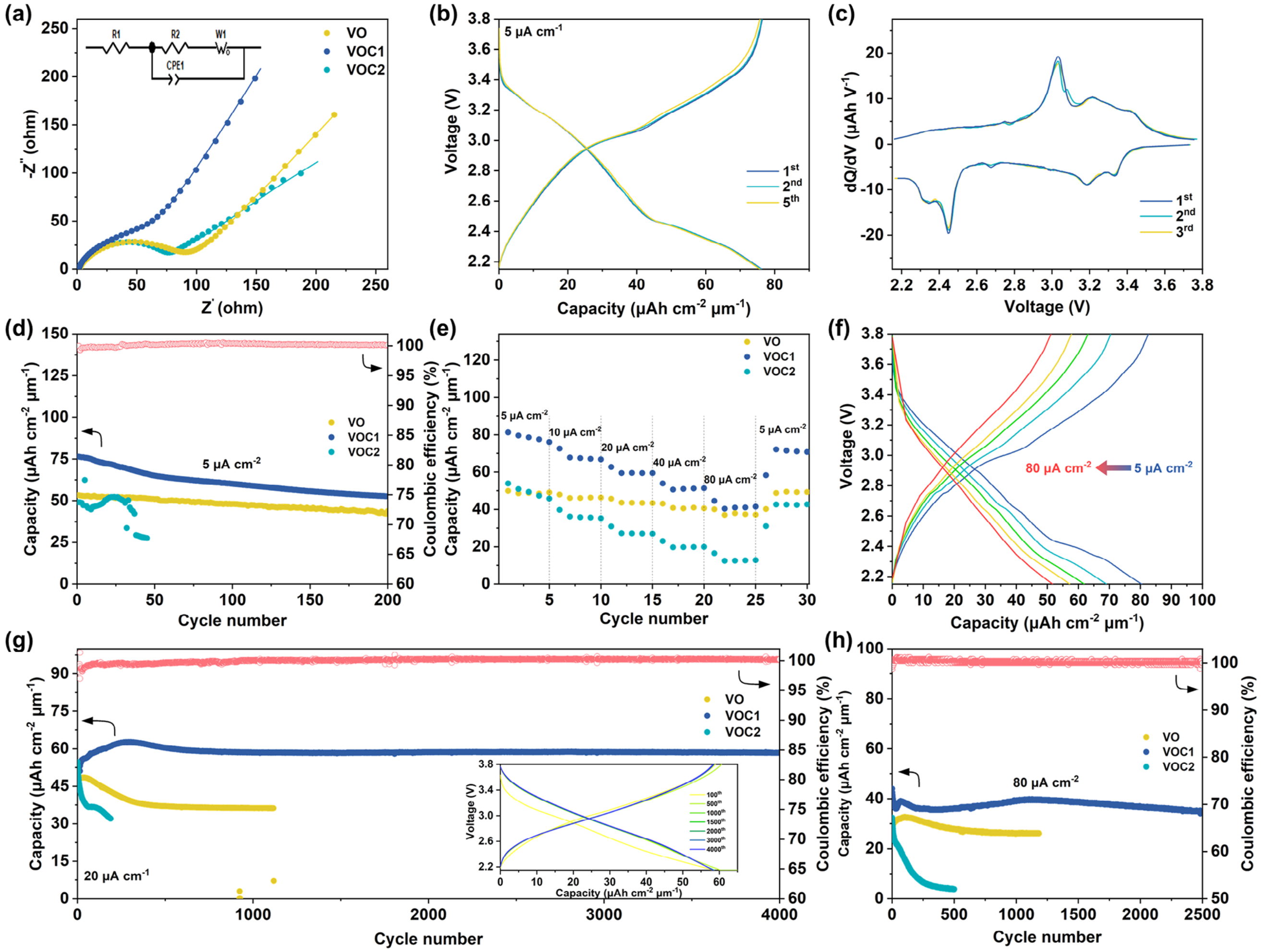

Figure 3. a) Fitted EIS patterns of VO, VOC1, and VOC2 electrodes. b) Galvanostatic charge/discharge profiles of the VOC1 electrode at the 1st, 2nd, and 5th cycles, respectively. c) Calculated dQ/dV profiles of VOC1 electrode for the first three cycles. d) Cycle performance comparison of the VO, VOC1, and VOC2 electrodes at 5 μA cm^{-2}. e) Rate capabilities of the VO, VOC1, and VOC2 electrodes, and f) corresponding galvanostatic charge/discharge profiles at the different specific currents. Long-term cycle performance g) at 20 μA cm^{-2} and h) at 80 μA cm^{-2}.

and O_2V^+ fragment and corresponding depth profiling curves shown in Figure 2f,g. This result can be accounted for by the presence of an oxygen partial pressure gradient during the annealing process, giving rise to an enrichment of V_2O_5, which is more prone to crystallize at 573 K, at the film surface.

2.2. Electrochemical Performance Evaluation

To understand the differences between VO, VOC1, and VOC2 cathodes in terms of their Li^+ storage ability, electrochemical properties were evaluated using liquid electrolyte-containing coin-type half-cells with a Li-metal anode (**Figure 3**). The electrochemical impedance spectra (EIS) of the three electrodes were recorded at open-circuit potential. As shown in Figure 3a and Table S1 (Supporting Information), the charge transfer resistance of the VOC1 electrode, determined through EIS fitting, is the lowest among the three electrodes at 62.45 Ω, which demonstrates the enhanced charge transfer efficiency by the V_2O_5-$Cu_2V_2O_7$ heterostructure. Although the charge transfer resistances of VOC1 and VOC2 are similar, the semicircle of VOC1 is incomplete in the high-frequency region, which is caused by the heterostructure that improves the mass-transfer efficiency at the V_2O_5-$Cu_2V_2O_7$ interface as well as at the whole electrode. Furthermore, VOC1 shows capacitive behavior with a larger slope of the straight line in the low-frequency region, which is attributed to the fact that the enrichment of V_2O_5 on the film surface enhances the ionic transport at the electrode/electrolyte interface, and thus the impedance value of Li^+ diffusion at the interface is lower. The capacitive behavior of VOC1 was further explored by Cyclic Voltammetry (CV) test at different scan rates between 0.1–1.0 mV s^{-1} (Figure S8, Supporting Information). Conversely, the slope of the VOC2 Warburg impedance is small, indicating that Li^+ diffusion at the electrode surface is hindered.[35] The EIS tests at different states of charge are shown in Figure S9 (Supporting Information), where VOC1 still exhibits excellent electrochemical kinetics during discharge from open-circuit to 2.15 V.

The galvanostatic charge–discharge curves between 2.15 and 3.8 V of the VO electrode at a current density of 5 µA cm^{-2} are given in Figure S10a (Supporting Information), with three typical discharge plateaus located at ≈3.4 V, ≈3.2 V, and ≈2.3 V (coinciding to the redox peaks in CV and dQ/dV curves in Figures S11a and S12a, Supporting Information), which correspond to the generation of ϵ-Li$_{0.5}$V$_2$O$_5$, δ-LiV$_2$O$_5$, and γ-Li$_2$V$_2$O$_5$, respectively, from α-V$_2$O$_5$ after insertion of Li$^+$. The initial discharge-specific capacity of the VO electrode is 53.3 µAh cm^{-2} µm^{-1}. As shown in Figure 3b, the initial charge/discharge profiles of the Li//VOC1 half-cell exhibit a prominent discharge plateau at ≈2.5 V as well as three smaller discharge plateaus located at ≈3.4, ≈3.2, and ≈2.3 V, respectively, which are more distinctly represented in the dQ/dV plot in Figure 3c. The latter is similar to the charge/discharge plateau of the VO electrode, originating from the gradual reduction of V^{5+} to V^{4+}, while the former ≈2.5 V discharge plateau is attributed to the reduction of Cu^{2+}.[31] As a result, VOC1 is capable of storing more Li$^+$ with a specific capacity of up to 76.4 µAh cm^{-2} µm^{-1} at the first cycle, which is a tremendous enhancement of 44% compared to the VO electrode. Unexpectedly, the redox peaks of the CV curves of the VOC1 electrode were not very distinct, which might be related to the slower diffusion rate of Li$^+$ in the Cu$_2$V$_2$O$_7$ phase, and the mass transfer rate could not satisfy the sufficient electrochemical reaction, and thus the redox peaks were not obvious. On the other hand, the current is fixed during the testing of the dQ/dV curve, so the diffusion rate is constant, the redox reaction is carried out completely, and therefore the potential change obtained is relatively accurate.[36,37] Surprisingly, the practical initial discharge specific capacity of the VOC2 electrode, which theoretically should be higher, was only 49.0 µAh cm^{-2} µm^{-1}, as shown in Figure S10b (Supporting Information). The discharge plateau commences at ≈3.4 V and the curve is more skewed, in addition to the absence of an explicit redox peak in the CV curve, which is related to the amorphous structure presented in VOC2. The charging plateau does not appear until the voltage reaches ≈3V. In order to demonstrate that it is too high current density that leads to a much lower VOC2 capacity than the ideal case, we performed low-current activation at 3 µA cm^{-2} for various electrodes. As depicted in Figure S13 (Supporting Information), only the initial specific capacity of VOC2 dramatically increased to 138.2 µAh cm^{-2} µm^{-1} and rapidly decreased at the third cycle. In addition, the charge/discharge curves of VOC2 fluctuated severely due to the irreversible phase changes during the possible conversion process (e.g., CuO→Cu+Li$_2$O). The low ion diffusion coefficient induces elevated concentration polarization, manifested as voltage dips, while the metallic Cu phase formed during conversion reactions mitigates ohmic polarization through enhanced electronic conductivity, resulting in partial voltage recovery. However, insulating by-products may restrict ion diffusion pathways, driving dynamic polarization fluctuations.

The structure stabilities of the various electrodes were further examined through cycling tests. Figure 3d presents a comparison of the cycling performance between 2.15 and 3.8 V at a current density of 5 µA cm^{-2}. It is clear that VOC2 suffers from rapid capacity fading and instability, retaining only ≈56% of its capacity after 45 cycles, indicating its poor structural stability and reversibility. In contrast, VO has better cyclic stability, gradually decaying to ≈82% capacity after 200 cycles, but with a lower capacity. As anticipated, the VOC1 electrode exhibited the highest specific capacity along with commendable cycling stability, retaining ≈69% after 200 cycles. To investigate the origin of the capacity fading, SEM was carried out to observe the surface of each electrode after cycling, as shown in Figure S14 (Supporting Information). Both VO and VOC2 show varying degrees of cracking and roughening. While the surface of VOC1 is still smooth, it shows an obvious regional contrast difference, which may be the electron channeling contrast caused by the different crystal orientations produced after cycling.[38]

The rate capabilities of the three electrodes are compared in Figure 3e. Layered V$_2$O$_5$, possessing a large layer spacing, could facilitate the rapid diffusion of Li$^+$ through 2D channels. The capacity of the VO electrode, however, is always at a lower value. As mentioned before, VOC2 shows a high specific capacity only at low current densities because of its extremely slow reaction kinetics. When Cu$_2$V$_2$O$_7$ is stabilized in a heterostructure based on V$_2$O$_5$, the VOC1 electrode demonstrates a high specific capacity and optimized rate performance, which is still greater than the of the VO electrode (37.9 µAh cm^{-2} µm^{-1}) even at a high current density of 80 µA cm^{-2} with an average specific capacity of 41.7 µAh cm^{-2} µm^{-1}. The corresponding charge/discharge curves of VOC1 at different current densities are shown in Figure 3f and Figure S15 (Supporting Information), which reveals that the stability of the VOC1 electrode has been promoted well along with high capacity.

As the VOC1 electrode was subjected to prolonged cycling at 20 µA cm^{-2} (Figure 3g), the maximum capacity is 62.7 µAh cm^{-2} µm^{-1} and ≈93% of the highest capacity can be retained after 4000 cycles, significantly surpassing the performance of previously reported V$_2$O$_5$-based cathodes (Table S2, Supporting Information), and even better than thin-film cathodes have been reported to our knowledge (Figure S16, Supporting Information). The insert figure shows the charge/discharge curves for a specific number of cycles, and we note that there is a capacity rise at the beginning, which may be caused by the continuous optimization of the heterostructure interface with the charging/discharging process. Significantly, the prevalent phenomenon of rapid capacity fading during initial cycling reported in the literature for Cu$_2$V$_2$O$_7$-based electrodes[39] was not observed for VOC1 heterostructured electrodes in this study, suggesting that the stability of the heterostructures is greatly elevated. On increasing the current to 80 µA cm^{-2} for long cycling, the VOC1 electrode still exhibits excellent stability and large capacity, with an initial specific capacity of 44.0 µAh cm^{-2} µm^{-1} and retaining ≈79% after 2500 cycles. To verify the repeatability and reproducibility of this work, we performed extensive repeat experiments for the main electrochemical results and collected duplicate data for valid statistical analysis (Figure S17, Supporting Information). The results corroborate the effective enhancement of electrochemical performance by the heterostructure.

2.3. Heterostructure and Ionic Storage Mechanism

To explore the mechanism underlying the remarkable electrochemical reversibility of the V$_2$O$_5$-Cu$_2$V$_2$O$_7$ heterostructure, in situ Raman measurements were performed on various electrodes to elucidate the potential-dependent reversible structural changes

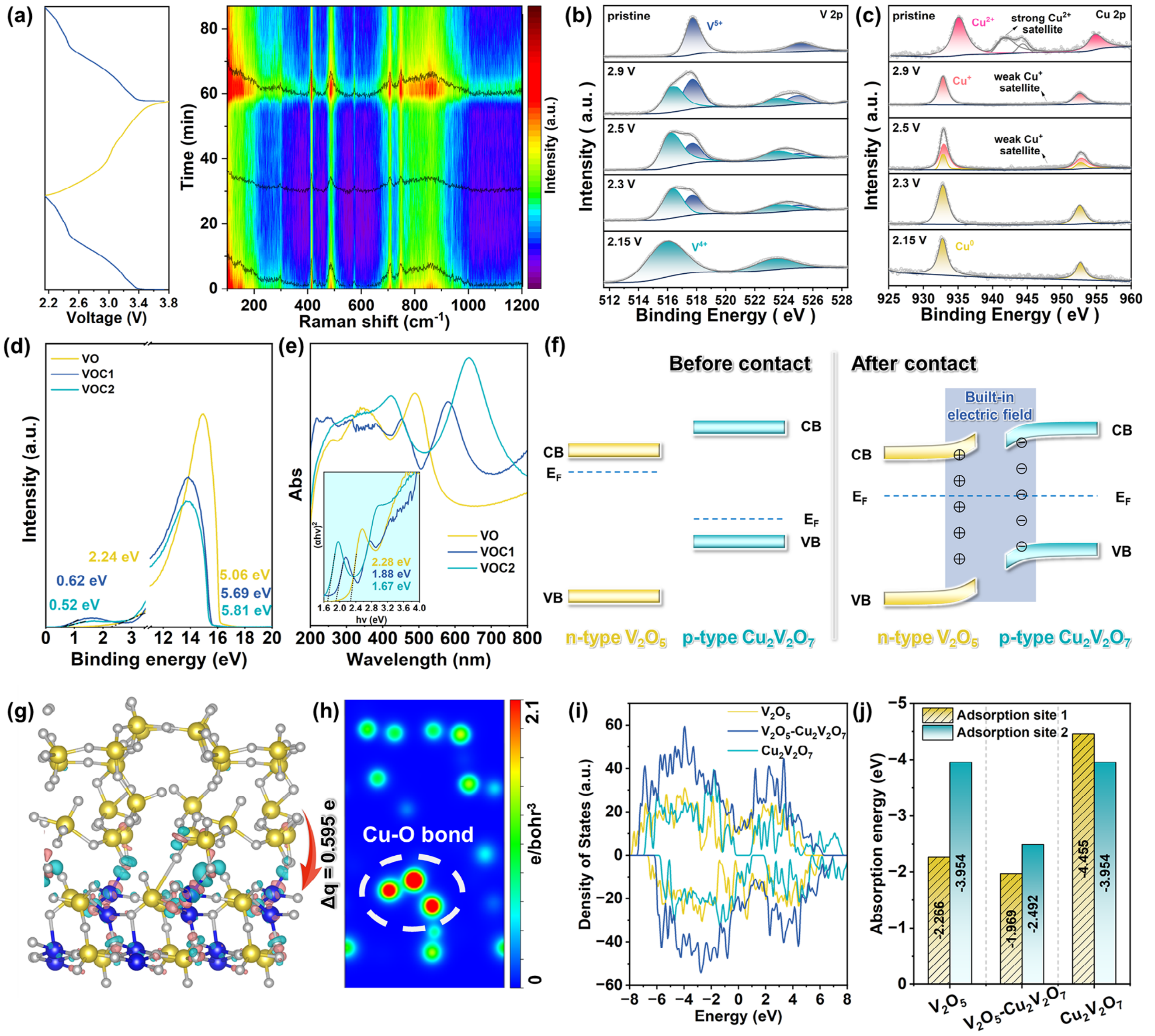

Figure 4. a) In situ Raman measurements of the VOC1 electrode in a voltage range between 2.15 and 3.8 V. b) V 2p, and c) Cu 2p ex-XPS spectra of VOC1 at the different lithiated states. d) UPS spectra, and e) UV–vis absorption spectroscopy of the VO, VOC1, and VOC2 thin films. f) The schematic illustration of the built-in electric field between V_2O_5 and $Cu_2V_2O_7$. g) The computed charge density difference and h) the corresponding 2D slice of the charge density of the V_2O_5-$Cu_2V_2O_7$ heterojunction. The pink and green isosurfaces represent charge accumulation and depletion in the space, respectively. i) The DOS and j) the adsorption energy values of Li-V_2O_5, the Li-V_2O_5-$Cu_2V_2O_7$ heterostructure, and Li-$Cu_2V_2O_7$.

and the VO bonding characteristic evolutions (**Figure 4a**; Figure S18, Supporting Information). The broad, low-intensity Raman peaks compared to the classic Raman spectrum of VOC1 thin film indicated the fluorescence effect from the addition of the electrolyte, which has been confirmed in previous reports.[40,41] The lowest Raman shift peak at 145 cm^{-1} involves the shear motion and rotations of the ladders along their axes. The pronounced intensity of this peak indicates the presence of long-range order within the vanadium-oxygen layers.[42] As can be discerned from the figure, the intensity of the 145 cm^{-1} mode decreases significantly during the discharge process, and the intensity of other peaks also decays significantly until discharged to 2.15 V with a minimum, suggesting that with the embedding of Li$^+$ leading to the inhibition of the interactions in the V—O$_1$, V—O$_2$, and V—O$_3$ bonds.[43] As a consequence, the disorder within the V_2O_5 layer increases. On the other hand, with progressive charging up to 3.8 V, the intensities of the peaks re-reach maximal value and weakened again during the second discharge, and the intercalation/expression of Li$^+$ did not entail apparent alteration of the bonding characteristics, which revealed the excellent structural stability and reversibility of the VOC1 electrode. Indeed, it is evident that the local distortions within the V_2O_5 structure are relatively mild, which allows it to accommodate up to 2 Li mol^{-1} of oxide, endowing it with superior reversibility.

The ex-situ XPS was executed to study the Li^+ storage capacity of the VOC1 electrode, at the pristine state, lithiated to 2.9, 2.5, and 2.3 V, and fully lithiated to 2.15 V, respectively (Figure 4b,c). When in the pristine state, the V_2O_5-$Cu_2V_2O_7$ heterostructure contains only V^{5+} and Cu^{2+}. However, when lithiated to 2.9 V, VOC1 presents ≈48% of V^{4+} in addition to V^{5+}, and the entire Cu^{2+} is reduced to Cu^+. This discloses that in addition to the presence of the reduction of V^{5+} at the 3.4 and 3.2 V discharge plateaus in the electrochemical tests, this stage also includes a capacity contributed by the reduction of all Cu^{2+} to Cu^+. Continuing the lithiation to 2.5 V, the proportion of V^{4+} increases and some of the Cu^+ is further reduced to Cu^0 until all of them transform to Cu^0 at 2.3 V, which corresponds to the peak located at 2.5 V in the dQ/dV curve. Eventually after complete lithiation at 2.15 V, the electrode contains only V^{4+} and Cu^0. Therefore, the enhanced capacity of the VOC1 electrode compared to the VO electrode originates from the gradual reduction of Cu^{2+} to Cu^0.

Based on the ultraviolet photoelectron spectroscopy (UPS) (Figure 4d) and the UV–vis absorption spectroscopy (Figure 4e), the proposed schematic energy-level diagrams for VO, VOC1, and VOC2 are illustrated in Figure S19 (Supporting Information). As VO has a lower work function (5.06 eV) as compared to that of VOC2 (5.81 eV), thus electrons are inclined to transfer from V_2O_5 to $Cu_2V_2O_7$ across the interface in the V_2O_5-$Cu_2V_2O_7$ heterostructure as briefly depicted in Figure 4f. The electron flow leads to the accumulation of positive and negative charges on each side of the interface. Meanwhile, the energy levels of V_2O_5 and $Cu_2V_2O_7$ bend near the interface until their Fermi levels achieve equilibrium. Bearing in mind that the $Cu_2V_2O_7$ domains are distributed randomly in the V_2O_5 matrix, Li^+ is required to diffuse from V_2O_5 into $Cu_2V_2O_7$ during the electrode lithiation process. The formed built-in electric field can accelerate Li^+ transport in this process. Specifically, Li^+ is attracted and accumulates on the $Cu_2V_2O_7$ side of the hetero-interface, and the built-in electric field may eventually vanish after charge equilibrium.[44] During the delithiation process, Li^+ in V_2O_5 is first extracted due to the rapid Li^+ migration properties of its layered structure. As the Li^+ in V_2O_5 continues to leach rapidly, a concentration gradient will be formed until the driving force required to break the charge equilibrium of the built-in electric field is exceeded, after which the built-in electric field will be reconstructed.[45] Overall, the reversibly formed built-in electric field accelerates the diffusion of Li^+ at the interface of the heterostructure and significantly facilitates the electrode kinetics, allowing the advantages of high specific capacity and excellent cycling stability of VOC1 to be demonstrated.

DFT calculations were performed to elucidate the principle of Li^+ storage kinetics at the V_2O_5-$Cu_2V_2O_7$ heterojunction. The charge density difference and the electron localization function (ELF) were then calculated individually. The V_2O_5 (101)-$Cu_2V_2O_7$ (200) heterostructure model (Figure S20, Supporting Information) was first optimized. Upon heterojunction formation, electrons are transferred from the V_2O_5 side to the $Cu_2V_2O_7$ side with an unbalanced charge distribution (Figure 4g,h), which probably induces the construction of a built-in electric field. ELF calculations reveal a decrease in the degree of electron localization at the interface after heterojunction formation (the color changes from red to blue), which suggests that the degree of delocalization at the interface is elevated (Figure S21, Supporting Information). Combined with the charge density difference, it demonstrates that the built-in electric field formed by the heterojunction delocalizes the electrons and facilitates the ion/electron transport. To support such a statement, the density-of-states (DOS), the Li^+ adsorption energy, and the Li^+ diffusion barrier were further calculated. Compared with V_2O_5, the V_2O_5-$Cu_2V_2O_7$ heterostructure exhibits stronger metallic properties and higher DOS strength (Figure 4i; Figure S22, Supporting Information). The band gap of the heterojunction is dramatically decreased after the formation of the heterojunction. The energy structure of the density of states is shifted due to the alignment of the Fermi energy levels. The comparison reveals an increase in the top electron density of the valence band at the $Cu_2V_2O_7$ side (the blue dashed box portion), which, in combination with the charge difference density results, suggests that the electrons migrate from the n-type semiconductor (V_2O_5) to the p-type semiconductor ($Cu_2V_2O_7$) side. Since the V_2O_5-$Cu_2V_2O_7$ heterostructure has a more appropriate Li^+ adsorption energy and lower Li^+ diffusion barrier, Li^+ can be readily adsorption/desorption and rapidly migrate within the heterostructure-based cathode (Figure 4j; Figures S23 and S24, Supporting Information). Thus, the V_2O_5-$Cu_2V_2O_7$ nanoheterostructure engenders a built-in electric field due to the imbalance charge distribution, concurrently elevating the degree of electron delocalization, which further optimizes the electronic conductivity, the adsorption energy and diffusion energy barriers for Li^+, and ultimately facilitates the faster charge transfer kinetics of Li^+ at the heterostructure interface and even in the whole VOC1 cathode.

2.4. All-Solid-State Thin-Film Battery

Since the limited active material loading capability of ATFBs, the cathode material with low volumetric specific capacity renders the capacity and stability of the whole battery at a disadvantage, which is antithetical to the market application.[46–48] Herein, the VOC1 electrode with unleashed capacity and optimized kinetics through heterostructure is expected to seek an ideal application in ATFBs. Most fundamentally, in order to determine the compatibility of the electrodes with the solid-state electrolyte before constructing the ATFBs, LiPON was deposited on the VOC1 thin film. As illustrated in the cross-section FESEM image (Figure S25, Supporting Information), the interface contact is well established, which guarantees efficient charge transfer at the interface with low interfacial resistance. Subsequently, ATFBs were fabricated with VO, VOC1, and VOC2 as the cathodes, LiPON as the solid-state electrolyte, and lithium metal as the anode, as illustrated in **Figure** 5a. Appropriate ionic conductivity (1.6×10^{-6} S cm^{-1}) and wide electrochemical window (≈5.0 V) with high stability make LiPON the most versatile solid-state electrolyte for ATFBs, which was RF sputtered using a Li_3PO_4 target in a pure N_2 atmosphere.[49–52] In the magnetron sputtering process, N_2 serves as both the sputtering gas and the active gas and is ionized into active particles at high pressure. The active particles react with the sputtered particles (atoms or groups of atoms in the Li_3PO_4 target) to produce LiPON.[53,54] The cross-section SEM images and corresponding EDS elemental mappings of ATFB are shown in Figure 5b,c, respectively. The well-separated and uniform distribution of elements such as V and Cu can be

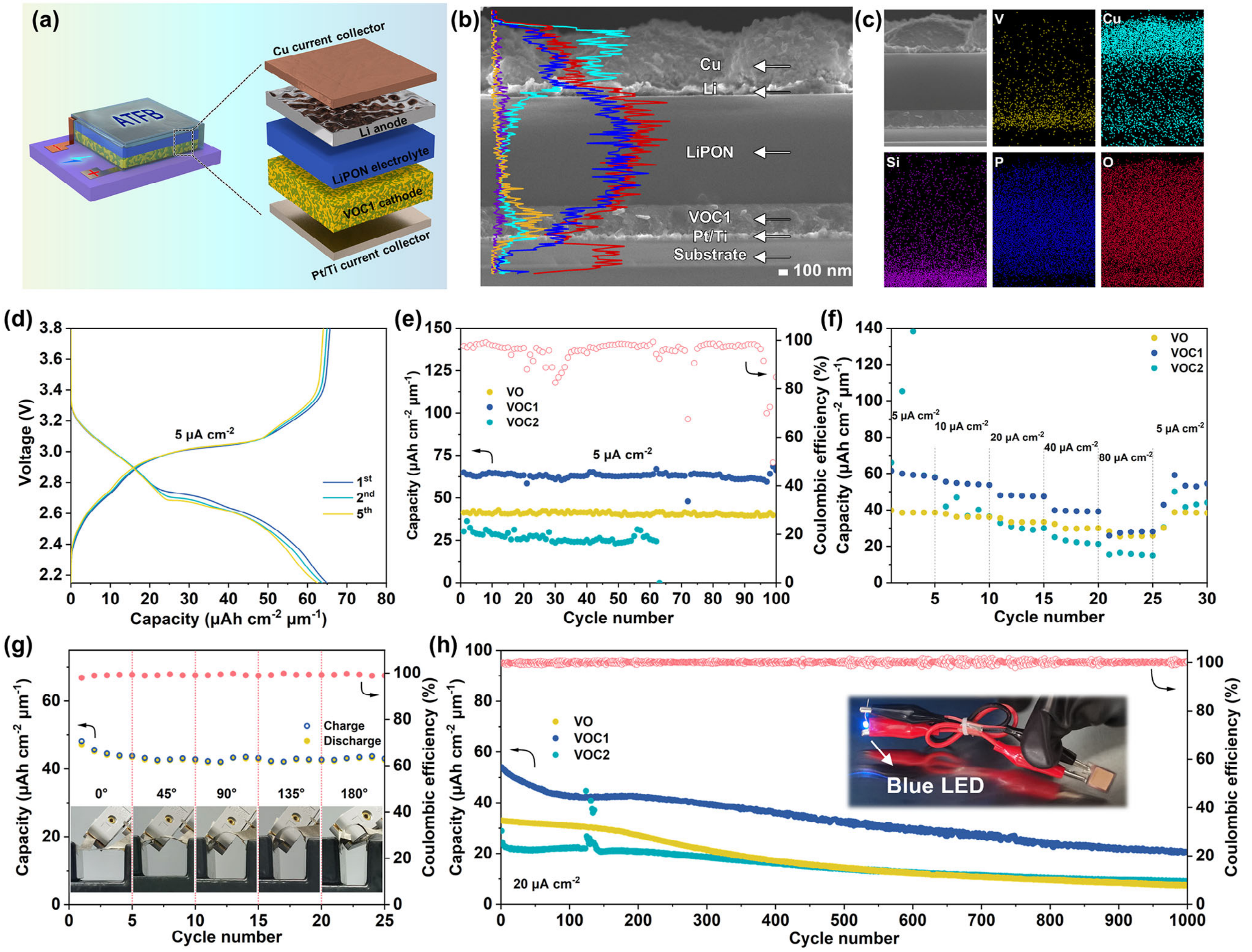

Figure 5. a) Schematic representation depicting the configuration of an all-solid-state thin-film battery. b) The cross-section FESEM image of the ATFB and corresponding EDS line scanning spectra. c) EDS elemental mappings of the ATFB. d) Galvanostatic charge/discharge profiles of ATFB based on the VOC1 cathode. e) Cycle performance comparison of the ATFBs at 5 μA cm^{-2}. f) Rate performance of the ATFBs. g) Cycle performance of the flexible ATFB at different bending states. h) Long-term cycle performance of ATFBs at 20 μA cm^{-2}. The inset shows the photo of blue-LED lit by an ATFB based on the VOC1 cathode.

explicitly observed, which further demonstrates the intimate interfacial contact.

The charge/discharge curves of the all-solid-state thin-film batteries constructed based on VO, VOC1, and VOC2 electrodes are shown in Figures 5d; S26, Supporting Information. The presented electrochemical features are similar to those in the half-cells, which can be more clearly visualized in the CV and dQ/dV curves of the thin-film batteries (Figures S27 and S28, Supporting Information). At a low current density of 5 μA cm^{-2}, the heterostructure-based ATFB exhibits a substantially optimized initial capacity of 65.0 μAh cm^{-2} $μm^{-1}$ compared to 41.3 μAh cm^{-2} $μm^{-1}$ for the VO. The capacity was still retained at 63.7 (≈98%) after 100 cycles, as shown in Figure 5e. Figure 5e,f,h illustrate that the specific capacity, rate performance, and stability of the ATFBs are relatively lower than those of the half-cells tested in the organic electrolyte, revealing the limited charge transfer kinetics of the solid-state battery architecture with LiPON as the electrolyte.[55] Nevertheless, the constructed thin-film batteries are substrate-selective-free and able to be perfectly constructed on including, but not limited to, quartz, silicon wafers, and stainless-steel foil. In addition, benefiting from the low annealing temperature of 573 K, the ATFB can be also fabricated on the ultrathin polyimide film (5 μm thickness) (Figure S29, Supporting Information). As a consequence, this ATFB is flexible and robust, with negligible capacity changes through various angles from 0° to 180° of in situ bending during galvanostatic charging and discharging of the battery (Figure 5g). Significantly, based on the high voltage advantage of vanadium oxides, the thin-film battery successfully lit up a 3.5 V blue light-emitting diode (Figure 5h inset). The initial capacity was 54.0 μAh cm^{-2} $μm^{-1}$ even at a high current density of 20 μA cm^{-2} and could be cycled for 1000 cycles, demonstrating the great potential of heterostructures for boosting the electrochemical performance and applications of all-solid-state thin-film batteries.

According to the galvanostatic charge/discharge curves in Figure 5d, the all-solid-state thin-film battery based on the V_2O_5-

$Cu_2V_2O_7$ heterostructure can provide an energy of ≈51 μWh. In addition, compared to all-solid-state thin-film batteries based on conventional cathode materials, such as $LiCoO_2$, $LiMn_2O_4$, and $LiFePO_4$, ATFBs based on VOC1 cathode can achieve superior electrochemical performance, especially in terms of specific capacity, energy density, rate performance, and cycle stability (Figure S30, Supporting Information).[47,56,57] Most notably, the annealing temperature of VOC1 cathode is only 573 K, which is considerably lower than the high annealing temperature of conventional cathode materials (typically higher than 773 K), saving the thin-film batteries from severe thermal damage during the on-chip integration process.

3. Conclusion

In conclusion, we propose a strategy of introducing Cu heteroatom via co-sputtering in V_2O_5 to in situ generating V_2O_5-$Cu_2V_2O_7$ heterostructures. The approach fully equilibrates the dual advantages of high voltage and large capacity of the electrode and greatly inflates the Li^+ storage capacity of the electrode. With the reasonable design of the heterostructure, the introduced built-in electric field promotes the rapid migration of electrons and ions, enhancing the charging/discharging efficiency and stability of the electrode. Theoretical calculations indicate that the charge redistribution and the interfacial electron delocalization reduce the charge transport resistance and further boost the comprehensive performance of the electrode. Consequently, V_2O_5-$Cu_2V_2O_7$ heterostructured cathode delivered a reversible specific capacity as high as 76.4 $\mu Ah\ cm^{-2}\ \mu m^{-1}$ at 5 $\mu A\ cm^{-2}$ and a superior capacity retention of ≈93% after 4000 cycles (20 $\mu A\ cm^{-2}$; 298±2 K) in the organic electrolyte. The constructed ATFB also has a large specific capacity of up to 65.0 $\mu Ah\ cm^{-2}\ \mu m^{-1}$, good rate performance, and excellent flexibility. This study demonstrated the effective improvement of vanadium oxide cathode capacity through heterostructure design and provided a novel insight into the design of high-capacity, integratable all-solid-state thin-film batteries for practical IoT terminal applications.

Supporting Information

Supporting Information is available from the Wiley Online Library or from the author.

Acknowledgements

This work was supported by the National Natural Science Foundation of China (No. U23A20555), and the National Energy-Saving and Low-Carbon Materials Production and Application Demonstration Platform Program (TC220H06N).

Conflict of Interest

The authors declare no conflict of interest.

Data Availability Statement

The data that support the findings of this study are available from the corresponding author upon reasonable request.

Keywords

heterostructure, high capacity, magnetron sputtering, thin film batteries, vanadium pentoxide

Received: December 7, 2024
Revised: March 28, 2025
Published online:

---

[1] V. Iyer, H. Gaensbauer, T. L. Daniel, S. Gollakota, *Nature* **2022**, *603*, 427.
[2] M. Zhu, O. G. Schmidt, *Nature* **2021**, *589*, 195.
[3] J. H. Pikul, H. Ning, *Joule* **2018**, *2*, 1036.
[4] W. Yang, L. Xu, W. Luo, M. Huang, K. Fu, R. Song, C. Han, R. Tu, J. Shi, L. Mai, *Matter* **2023**, *6*, 3006.
[5] Y. Zhu, J. C. Gonzalez-Rosillo, M. Balaish, Z. D. Hood, K. J. Kim, J. L. M. Rupp, *Nat. Rev. Mater.* **2021**, *6*, 313.
[6] M. Balaish, J. C. Gonzalez-Rosillo, K. J. Kim, Y. Zhu, Z. D. Hood, J. L. M. Rupp, *Nat. Energy* **2021**, *6*, 227.
[7] Q. Xia, F. Zan, J. Xu, W. Liu, Q. Li, Y. He, J. Hua, J. Liu, Q. Zhang, J. Wang, C. Wu, H. Xia, *Adv. Mater.* **2023**, *35*, 2200538.
[8] L. Wang, Z. Wu, J. Zou, P. Gao, X. Niu, H. Li, L. Chen, *Joule* **2019**, *3*, 2086.
[9] J. Lin, L. Lin, S. Qu, D. Deng, Y. Wu, X. Yan, Q. Xie, L. Wang, D. Peng, *Energy Environ. Mater.* **2022**, *5*, 133.
[10] M. S. Whittingham, *Chem. Rev.* **2004**, *104*, 4271.
[11] P. Sun, X. Li, J. Shao, P. V. Braun, *Adv. Mater.* **2021**, *33*, 2006229.
[12] P. Hu, P. Hu, T. D. Vu, M. Li, S. Wang, Y. Ke, X. Zeng, L. Mai, Y. Long, *Chem. Rev.* **2023**, *123*, 4353.
[13] C.-F. Xiao, J. H. Kim, S.-H. Cho, Y. C. Park, M. J. Kim, K.-B. Chung, S.-G. Yoon, J.-W. Jung, I.-D. Kim, H.-S. Kim, *ACS Nano* **2021**, *15*, 4561.
[14] Y. Zhang, Y. Luo, C. Fincher, S. Banerjee, M. Pharr, *J. Mater. Chem. A* **2019**, *7*, 23922.
[15] E. Østreng, K. B. Gandrud, Y. Hu, O. Nilsen, H. Fjellvåg, *J. Mater. Chem. A* **2014**, *2*, 15044.
[16] A. Sakunthala, M. V. Reddy, S. Selvasekarapandian, B. V. R. Chowdari, P. C. Selvin, *Energy Environ. Sci.* **2011**, *4*, 1712.
[17] V. C. Ferrari, N. S. Kim, S. B. Lee, G. W. Rubloff, D. M. Stewart, *J. Mater. Chem. A* **2022**, *10*, 12518.
[18] S.-H. Park, P. J. King, R. Tian, C. S. Boland, J. Coelho, C. (John) Zhang, P. McBean, N. McEvoy, M. P. Kremer, D. Daly, J. N. Coleman, V. Nicolosi, *Nat. Energy* **2019**, *4*, 560.
[19] N. Wang, X. Zhang, Z. Ju, X. Yu, Y. Wang, Y. Du, Z. Bai, S. Dou, G. Yu, *Nat. Commun.* **2021**, *12*, 4519.
[20] T. Wei, B. Y. Ahn, J. Grotto, J. A. Lewis, *Adv. Mater.* **2018**, *30*, 1703027.
[21] Z. Wang, Y. Song, J. Wang, Y. Lin, J. Meng, W. Cui, X. Liu, *Angew. Chem., Int. Ed.* **2023**, *62*, 202216290.
[22] X. Wang, Y. Li, S. Wang, F. Zhou, P. Das, C. Sun, S. Zheng, Z. Wu, *Adv. Energy Mater.* **2020**, *10*, 2000081.
[23] Y. Gao, X. Nan, R. Zhao, B. Sun, W. Xu, Q. Li, Y. Cong, Y. Li, W. Lv, Q. Zhang, X. Li, N. Yang, *Adv. Funct. Mater.* **2023**, https://doi.org/10.1002/adfm.202310117.
[24] Y. Li, J. Zhang, Q. Chen, X. Xia, M. Chen, *Adv. Mater.* **2021**, *33*, 2100855.
[25] T. Wang, J. He, Z. Zhu, X.-B. Cheng, J. Zhu, B. Lu, Y. Wu, *Adv. Mater.* **2023**, *35*, 2303520.
[26] Z. Ye, Y. Jiang, L. Li, F. Wu, R. Chen, *Adv. Mater.* **2021**, *33*, 2101204.
[27] P. Shvets, O. Dikaya, K. Maksimova, A. Goikhman, *J. Raman Spectrosc.* **2019**, *50*, 1226.
[28] D. De Waal, C. Hutter, *Mater. Res. Bull.* **1994**, *29*, 843.
[29] Y. Wei, K. Nam, G. Chen, C. Ryu, K. Kim, *Solid State Ion* **2005**, *176*, 2243.

[30] J. D. Hanawalt, H. W. Rinn, L. K. Frevel, *Ind. Eng. Chem. Anal. Ed.* **1938**, *10*, 457.
[31] W. Guo, X. Lian, Y. Nie, M. Hu, L. Wu, H. Gao, T. Wang, *Mater. Lett.* **2020**, *258*, 126842.
[32] E. Marenkov, K. Nordlund, I. Sorokin, A. Eksaeva, K. Gutorov, J. Jussila, F. Granberg, D. Borodin, *J. Nucl. Mater.* **2017**, *496*, 18.
[33] W. Eckstein, J. Roth, W. Nagel, R. Dohmen, *J. Nucl. Mater.* **2004**, *328*, 55.
[34] F. Cheng, J. Chen, *J. Mater. Chem.* **2011**, *21*, 9841.
[35] A. E. Bumberger, A. Nenning, J. Fleig, *Phys. Chem. Chem. Phys.* **2024**, *26*, 15068.
[36] D. Li, L. Dai, X. Ren, F. Ji, Q. Sun, Y. Zhang, L. Ci, *Energy Environ. Sci.* **2021**, *14*, 424.
[37] P. Gao, Q. Ru, Z. Pan, J. Zhang, W. Xu, F. Chi-Chung Ling, L. Wei, *J. Colloid Interface Sci.* **2021**, *599*, 730.
[38] S. Kaboli, D. Goldbaum, R. R. Chromik, R. Gauvin, *Microsc. Microanal.* **2013**, *19*, 1620.
[39] Y. Wang, L. Cao, J. Huang, L. Kou, J. Li, J. Wu, Y. Liu, L. Pan, *ACS Sustainable Chem. Eng.* **2019**, *7*, 6267.
[40] L. Cabo-Fernandez, A. R. Neale, F. Braga, I. V. Sazanovich, R. Kostecki, L. J. Hardwick, *Phys. Chem. Chem. Phys.* **2019**, *21*, 23833.
[41] A. Jarry, S. Gottis, Y.-S. Yu, J. Roque-Rosell, C. Kim, J. Cabana, J. Kerr, R. Kostecki, *J. Am. Chem. Soc.* **2015**, *137*, 3533.
[42] R. Baddour-Hadjean, C. Navone, J. P. Pereira-Ramos, *Electrochim. Acta* **2009**, *54*, 6674.
[43] Z. Zhang, W. Xie, J. Li, H. Zhang, Q. Wang, C. Zhang, G. Xu, J. Gao, A. A. Rogachev, H. Cao, *Adv. Mater. Interfaces* **2022**, *9*, 2200883.
[44] L. Fang, Z. Lan, W. Guan, P. Zhou, N. Bahlawane, W. Sun, Y. Lu, C. Liang, M. Yan, Y. Jiang, *Energy Storage Mater.* **2019**, *18*, 107.
[45] C. Zhang, F. Han, F. Wang, Q. Liu, D. Zhou, F. Zhang, S. Xu, C. Fan, X. Li, J. Liu, *Energy Storage Mater.* **2020**, *24*, 208.
[46] Y. Zhang, S. Zheng, F. Zhou, X. Shi, C. Dong, P. Das, J. Ma, K. Wang, Z. Wu, *Small* **2021**, *18*, 2104506.
[47] Q. Xia, S. Sun, J. Xu, F. Zan, J. Yue, Q. Zhang, L. Gu, H. Xia, *Small* **2018**, *14*, 1804149.
[48] H. Huang, J. He, Z. Wang, H. Zhang, L. Jin, N. Chen, Y. Xie, X. Chu, B. Gu, W. Deng, W. Yang, *Nano Energy* **2020**, *69*, 104431.
[49] A. C. Kozen, A. J. Pearse, C.-F. Lin, M. Noked, G. W. Rubloff, *Chem. Mater.* **2015**, *27*, 5324.
[50] M. Nisula, Y. Shindo, H. Koga, M. Karppinen, *Chem. Mater.* **2015**, *27*, 6987.
[51] N. Suzuki, S. Shirai, N. Takahashi, T. Inaba, T. Shiga, *Solid State Ion* **2011**, *191*, 49.
[52] Y.-W. You, J.-W. Cui, X.-F. Zhang, F. Zheng, S.-Q. Wu, Z.-Z. Zhu, *Acta Phys. Sin.* **2021**, *70*, 136801.
[53] W. Dai, Y. Qiao, Z. Ma, T. Wang, Z. Fu, *Mater. Futures* **2022**, *1*, 032101.
[54] J. D. LaCoste, A. Zakutayev, L. Fei, *J. Phys. Chem. C* **2021**, *125*, 3651.
[55] S. Sun, Z. Han, W. Liu, Q. Xia, L. Xue, X. Lei, T. Zhai, D. Su, H. Xia, *Nat. Commun.* **2023**, *14*, 6662.
[56] Q. Xia, Q. Zhang, S. Sun, F. Hussain, C. Zhang, X. Zhu, F. Meng, K. Liu, H. Geng, J. Xu, F. Zan, P. Wang, L. Gu, H. Xia, *Adv. Mater.* **2021**, *33*, 2003524.
[57] B. Ke, S. Cheng, C. Zhang, W. Li, J. Zhang, R. Deng, J. Lin, Q. Xie, B. Qu, L. Qiao, D. Peng, X. Wang, *Adv. Energy Mater.* **2024**, *14*, 2303757.